

Combining Superionic Conduction and Favorable Decomposition Products in the Crystalline Lithium–Boron–Sulfur System: A New Mechanism for Stabilizing Solid Li-Ion Electrolytes

Austin D. Sendek, Evan R. Antoniuk, Ekin D. Cubuk, Brandi Ransom, Brian E. Francisco, Josh Buettner-Garrett, Yi Cui, and Evan J. Reed*



Cite This: <https://dx.doi.org/10.1021/acsami.9b19091>



Read Online

ACCESS |



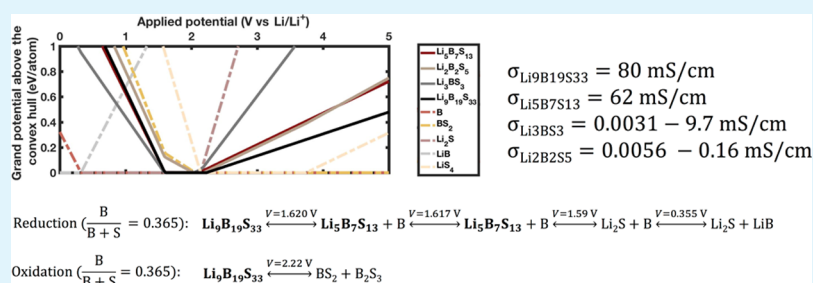
Metrics & More



Article Recommendations



Supporting Information



ABSTRACT: We report a solid-state Li-ion electrolyte predicted to exhibit simultaneously fast ionic conductivity, wide electrochemical stability, low cost, and low mass density. We report exceptional density functional theory (DFT)-based room-temperature single-crystal ionic conductivity values for two phases within the crystalline lithium–boron–sulfur (Li–B–S) system: 62 (+9, –2) mS cm^{–1} in Li₅B₇S₁₃ and 80 (–56, –41) mS cm^{–1} in Li₉B₁₉S₃₃. We report significant ionic conductivity values for two additional phases: between 0.0056 and 0.16 mS/cm^{–1} in Li₂B₂S₅ and between 0.0031 and 9.7 mS cm^{–1} in Li₃BS₃ depending on the room-temperature extrapolation scheme used. To our knowledge, our prediction gives Li₉B₁₉S₃₃ and Li₅B₇S₁₃ the second and third highest reported DFT-computed single-crystal ionic conductivities of any crystalline material. We compute the thermodynamic electrochemical stability window widths of these materials to be 0.50 V for Li₅B₇S₁₃, 0.16 V for Li₂B₂S₅, 0.45 V for Li₃BS₃, and 0.60 V for Li₉B₁₉S₃₃. Individually, these materials exhibit similar or better ionic conductivity and electrochemical stability than the best-known sulfide-based solid-state Li-ion electrolyte materials, including Li₁₀GeP₂S₁₂ (LGPS). However, we predict that electrolyte materials synthesized from a range of compositions in the Li–B–S system may exhibit even wider thermodynamic electrochemical stability windows of 0.63 V and possibly as high as 3 V or greater. The Li–B–S system also has a low elemental cost of approximately 0.05 USD/m² per 10 μm thickness, which is significantly lower than that of germanium-containing LGPS, and a comparable mass density below 2 g/cm³. These fast-conducting phases were initially brought to our attention by a machine learning-based approach to screen over 12,000 solid electrolyte candidates, and the evidence provided here represents an inspiring success for this model.

KEYWORDS: solid ion conductor, solid electrolyte, Li-ion battery, density functional theory, ion transport, electrochemical stability, kinetics

INTRODUCTION

All-solid-state Li-ion batteries (SSLIBs) hold promise as safer, longer-lasting, and more energy-dense alternatives to today's commercialized LIBs with liquid electrolytes. However, the discovery and design of suitable solid electrolyte materials for use in SSLIBs remains a significant engineering challenge. A high-performance solid electrolyte must simultaneously exhibit fast Li-ion conduction, negligible electronic conduction, and robust electrochemical stability. The material should also be made from cheap and low-mass elements in order to ensure cost competitiveness and high energy density. Ceramic materials are an attractive class of materials for this application,¹ but all ceramic lithium electrolyte materials

heretofore reported in the literature falter on at least one of these critical properties.² We report here evidence that solid electrolytes from the lithium–boron–sulfur (Li–B–S) chemical system display promising predicted values for all these properties, comparable to or exceeding those of the best-known ceramic electrolyte materials.

Received: October 22, 2019

Accepted: July 23, 2020

Published: July 23, 2020



A common discovery strategy for new solid electrolyte materials is to search chemical space for a material that simultaneously possesses fast ionic conduction and a wide electrochemical stability window. This strategy is guided by the empirical observation that electrolytes with an electrochemical stability window narrower than the potential difference across the electrodes undergo degradation reactions at the electrode–electrolyte interface (EEI) that result in interfacial products with typically poor ionic conductivity.³ These interfacial phases then block ionic motion between electrodes and halt battery operation. Typically, degradation passivates the electrode against further reaction, but degradation can continue until the entire electrolyte reacts if one or more of the EEI degradation products are electron conductors.

The material $\text{Li}_{10}\text{GeP}_2\text{S}_{12}$ (LGPS) is currently considered among the best available lithium-ion conductors, with an ionic conductivity of 12 mS cm^{-1} at room temperature (RT).⁴ Unfortunately, LGPS also exhibits a very narrow (thermodynamic) electrochemical stability window of approximately 0.3 V (2.1–2.4 V vs Li/Li^+).⁵ Computational and experimental studies have been reported that suggest that metallic and ionically insulating reaction products form on the lithium-metal anode interface when operated outside of this electrochemical stability window.^{5,6} Typical commercial LIBs exhibit a voltage difference of approximately 4 V across the cathode and anode (approximately 0.1–3.8 V vs Li/Li^+ for a graphite/transition-metal oxide cell),^{7,8} and thus, LGPS can only withstand a small fraction of the voltage range required for significant energy density.

Our recent work⁹ and work by Muy et al.¹⁰ suggest that ionic conductivity and electrochemical stability may be inversely correlated, suggesting that optimal materials are outliers and likely to be very difficult to find. More creative solutions may be required to circumvent this limitation. We propose an alternative approach to the strategy of searching for one material that simultaneously optimizes both criteria: identifying a high-ionic-conductivity solid material that breaks down into fast ion conducting and electronically insulating phases at both EEIs. In this scenario, a wider effective electrochemical window may be achieved because the electrolyte passes through more phase transitions before poor ion conductors actually appear. Realizing this strategy is an exercise in materials discovery: no existing materials appear to have this property, so new materials must be discovered.

Here, we predict that crystalline Li–B–S is a promising material system that may demonstrate this capability: we find evidence that phase mixtures of fast ion conducting phases from the Li–B–S system, $\text{Li}_5\text{B}_7\text{S}_{13}$, $\text{Li}_2\text{B}_2\text{S}_5$, Li_3BS_3 , and $\text{Li}_9\text{B}_{19}\text{S}_{33}$, over a range of boron-to-sulfur ratios will oxidize and reduce into ionically conducting and electronically insulating interfacial products, enabling electrochemical stability over a wider potential range than any of the individual phases alone.

Lithium-ion conducting glasses from the B_2S_3 – Li_2S system were discovered in the early 1980s and reported to have an RT lithium-ion conductivity of $10^{-4} \text{ S cm}^{-1}$.¹¹ Doping with LiI was reported to increase the lithium conductivity by an order of magnitude, but the oxidation of iodine resulted in a too narrow electrochemical stability window for use in SSLIBs.^{12,13} Sulfide-based glassy conductors also tend to be quite hygroscopic, which can present stability and performance issues in battery applications.¹⁴ The crystalline phases of the Li–B–S system and their solid solutions were first studied with Li NMR in the 1990s, including their ionic transport

properties, but we find no reports of ionic conductivity or electrochemical stability in these works.^{15–17}

We reinvestigate the Li–B–S system with today's *ab initio* simulation tools and materials databases at our disposal and find new evidence to suggest that these materials may be among the most promising solid Li-ion electrolyte materials. We report here evidence that four phases in the crystalline Li–B–S system exhibit a high RT bulk ionic conductivity ($\sim 10^{-2} \text{ S cm}^{-1}$), without the addition of iodine. Furthermore, a study of the thermodynamics of the phase diagram suggests that unlike any other known superionic lithium conductors, materials in the Li–B–S system may exhibit the valuable property of decomposing from one solid solution of superionic conductors to another upon oxidation and reduction. This suggests that an electrochemical stability window wider than that of a single sulfide phase may be realizable. Additionally, the low molecular weight and materials cost of Li–B–S materials may make them all the more attractive. We investigate the properties of this system below.

Ionic Conductivity. First, we perform an evaluation of the ionic conductivity of four phases in the Li–B–S system: $\text{Li}_5\text{B}_7\text{S}_{13}$, Li_3BS_3 , $\text{Li}_2\text{B}_2\text{S}_5$, and $\text{Li}_9\text{B}_{19}\text{S}_{33}$. We report that all four of these thermodynamically stable phases exhibit high lithium ion conduction at RT. These structures were initially characterized in the early 1990s as crystalline phases observed from Li–B–S glasses and have space groups *Cc*, *Pnma*, *Cmcm*, and *C2/c*, respectively.^{18–24} These phases were brought to our attention as potential Li-ion conductors by our machine learning-based superionic predictor model developed in a previous work.^{25,26} $\text{Li}_5\text{B}_7\text{S}_{13}$, Li_3BS_3 , $\text{Li}_2\text{B}_2\text{S}_5$, and $\text{Li}_9\text{B}_{19}\text{S}_{33}$ possess generally favorable values for the five structural features used by our machine-learned model to predict fast ion conduction: many lithium–lithium neighbors (2.7, 6.0, 4.0, 1.4, respectively, compared to a median value of 2.6 across over 10,000 Li-containing materials with characterized structures), small electronegativity difference between sublattice atoms (0.5, 0.9, 0.4, 0.4; a median of 0.9), low anion framework coordination numbers (7.7, 7.3, 5.2, 8.4; a median of 10), and large lithium-anion separation distance (2.5, 2.5, 2.6, 2.4 Å; a median of 2.0 Å). The fifth feature, the lithium–lithium separation distance, is relatively large (3.7, 3.2, 3.3, 3.6 Å; a median of 3.2), but this is compensated by the favorable values of the other four features. With these feature values, the machine learning-based model predicts these materials to exhibit superionic lithium conduction. Although some knowledge in the literature about ion transport in these materials predated our machine learning model, no information about the structure or conductivity of any Li–B–S materials was included in the model. This makes the model's predictions of fast ion conductivity in these phases true generalizations of the model. The computational observations of fast ion conduction we provide here suggest that all four predictions by the model may be correct, representing an exciting validation of our machine learning-based approach.

To predict the RT ionic conductivity in $\text{Li}_5\text{B}_7\text{S}_{13}$, $\text{Li}_2\text{B}_2\text{S}_5$, Li_3BS_3 , and $\text{Li}_9\text{B}_{19}\text{S}_{33}$, we perform density functional theory molecular dynamics (DFT-MD) on single crystals of these materials at 900, 700, 400, and 293 K. We leverage the Perdew–Burke–Ernzerhof (PBE)²⁷ methodology of the generalized gradient approximation (GGA) and the projector augmented wave (PAW) method.²⁸ Ionic diffusion in solids is generally not isotropic; this three-dimensional diffusivity value is equivalent to the mean of the diagonal elements of the

diffusion tensor or one-third of the trace. We refer the reader to the [Methods](#) section for discussion of the simulation details.

In [Figure 1](#), we plot the logarithm of ionic conductivity versus inverse temperature and confirm significant Li

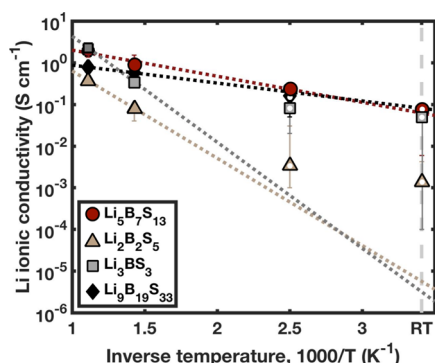


Figure 1. Temperature dependence of Li ionic conductivity. We simulate DFT MD at 900, 700, 400, and 293 K for four promising materials from the Li–B–S system, $\text{Li}_5\text{B}_7\text{S}_{13}$, $\text{Li}_2\text{B}_2\text{S}_5$, Li_3BS_3 , and $\text{Li}_9\text{B}_{19}\text{S}_{33}$. We compute the average Bader charge on Li and the slope of the Li MSD curves and then employ eqs 2 and 3 to compute the Li ionic conductivity. These values represent the average of the diagonal elements of the conductivity tensor. The diffusivity is determined from the slope of the MSD curve. The error bars represent the 75th and 25th percentiles of slopes in the diffusivity considering all time origins from 0 to 75% of the final run time in 100 equally spaced intervals. If the Arrhenius dynamics is assumed, the high-temperature ionic conductivity extrapolates to give the following RT ionic conductivities: 74 mS cm^{-1} for $\text{Li}_5\text{B}_7\text{S}_{13}$, $0.0056 \text{ mS cm}^{-1}$ for $\text{Li}_2\text{B}_2\text{S}_5$, $0.0031 \text{ mS cm}^{-1}$ for Li_3BS_3 , and 80 mS cm^{-1} for $\text{Li}_9\text{B}_{19}\text{S}_{33}$, respectively. This would make $\text{Li}_5\text{B}_7\text{S}_{13}$ and $\text{Li}_9\text{B}_{19}\text{S}_{33}$ over 5 times more conductive than LGPS and two of the fastest solid Li-ion conductors predicted to date. The markers with white dots at their centers denote simulations that did not reach an MSD of approximately 100 \AA^2 over the simulation period; we assume these results to not be converged and leave them out of the Arrhenius extrapolation.³⁰ If the 400 K simulations for $\text{Li}_2\text{B}_2\text{S}_5$, Li_3BS_3 , and $\text{Li}_9\text{B}_{19}\text{S}_{33}$ are factored into the extrapolations, the RT ionic conductivity predictions become the following: 0.16 mS cm^{-1} for $\text{Li}_2\text{B}_2\text{S}_5$, 9.7 mS cm^{-1} for Li_3BS_3 , and 56 mS cm^{-1} for $\text{Li}_9\text{B}_{19}\text{S}_{33}$.

conduction in all four materials at RT when the Arrhenius dynamics is assumed. The RT Li conductivity values of $\text{Li}_9\text{B}_{19}\text{S}_{33}$ and $\text{Li}_5\text{B}_7\text{S}_{13}$ in particular are remarkable: 80 (-56 , -41) and 62 ($+9$, -2) mS cm^{-1} , respectively. These are both several times higher than the reported DFT single-crystal RT ionic conductivity for LGPS (9 mS cm^{-1})²⁹ and the experimentally measured RT ionic conductivity of polycrystalline LGPS (12 mS cm^{-1}).⁴ The ionic conductivities of the other materials vary significantly depending on the details of the RT extrapolation: when the results from the 400 and 293 K simulations are removed from the extrapolations because of uncertain convergence,³⁰ the following RT ionic conductivities are calculated: 0.0056 (-0.0052 , -0.0056) mS cm^{-1} for $\text{Li}_2\text{B}_2\text{S}_5$ and 0.0031 ($+0.019$, -0.0023) mS cm^{-1} for Li_3BS_3 . When the results of the 400 K simulations are included, the following RT ionic conductivities are calculated: 0.16 (-0.05 , -0.14) mS cm^{-1} for $\text{Li}_2\text{B}_2\text{S}_5$ and 9.7 ($+4$, -8) mS cm^{-1} for Li_3BS_3 . To compute the uncertainties in these values, we extrapolate down to RT along the upper and lower limits of the high-temperature uncertainties. We refer the reader to the [Methods](#) section for further discussion of calculating the uncertainties.

These predictions for single crystals are among the highest DFT-predicted Li-ion conductivities in crystalline materials. We note that future experimental studies of ionic conductivity in these materials may be affected by defects, grain boundary resistance, and microstructure, none of which are incorporated into single-crystal DFT calculations. The impact of such effects on the overall conductivity is generally not predictable.

We compute the electronic band gaps of $\text{Li}_5\text{B}_7\text{S}_{13}$, $\text{Li}_2\text{B}_2\text{S}_5$, Li_3BS_3 , and $\text{Li}_9\text{B}_{19}\text{S}_{33}$ with PBE DFT to be 3.6, 2.4, 3.1, and 2.9 eV, respectively. Because PBE DFT simulations tend to underestimate the true band gap by a factor of 2 or more,³¹ we also compute the band gaps with the more accurate HSE06 hybrid functional³² with a single k -point; we report values of 4.7, 3.5, 4.2, and 4.0 eV, respectively. A high band gap in solid electrolyte materials is desired in order to minimize electrical conductivity and maximize electrochemical stability. Although the electrical conductivity depends on both the electronic density of states and the band gap, calculations for pure Si demonstrate that a true band gap of 1 eV or higher leads to acceptably small levels of electron conduction.²⁵ Assuming a minimum acceptable band gap of 1 eV, our calculations predict that the band gaps are sufficiently large for the Li–B–S phases to be useful in solid electrolyte applications. Furthermore, the band gap (in electronvolts) is an upper bound on the thermodynamic electrochemical stability window width (in volts),^{33,34} so larger band gaps may indicate more robust electrochemical stability. To execute these calculations, we leverage the Automatic-FLOW (AFLOW) for Materials Discovery k -point path generator^{35,36} and the P4VASP visualization tool. More details on these calculations are provided in the [Methods](#) section.

Reactions at the Electrode–Electrolyte Interface. The ternary Li–B–S phase diagram with thermodynamically stable phases is provided in [Figure 2](#). We note that the four fast-conducting phases discovered here are the only predicted stable phases on the interior of the phase diagram.

Knowing that there are four excellent lithium-ion conductors in the Li–B–S chemical space, the next step is to identify the optimal composition and operating range for use as an

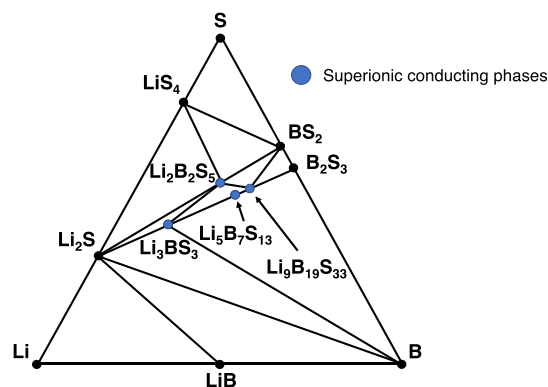


Figure 2. Ternary phase diagram of the Li–B–S system. We predict $\text{Li}_5\text{B}_7\text{S}_{13}$, $\text{Li}_2\text{B}_2\text{S}_5$, Li_3BS_3 , and $\text{Li}_9\text{B}_{19}\text{S}_{33}$ to be stable Li superionic conductors at RT. This suggests that at least one of these four superionic phases will be present in many possible $\text{Li}_x\text{B}_y\text{S}_z$ compositions, suggesting in turn that the Li–B–S system may exhibit fast Li-ion conduction even when the material composition changes *via* interfacial degradation. The discovery of additional stable phases and their incorporation onto this phase diagram may evolve this conclusion.

electrolyte. This requires predicting the phases that will form at arbitrary composition $x\text{Li} + y\text{B} + z\text{S}$ as well as which phases will result when the electrolyte is oxidized/reduced by the cathode/anode at the EEI. Existing methods for computationally predicting the electrochemical stability of electrolyte materials rely exclusively on thermodynamic considerations.^{5,37,38} This approach is valuable for predicting the possible interfacial behavior but neglects the potentially important kinetics. We first examine the thermodynamics and then return to the kinetics in the following section.

The thermodynamic approach to predicting the electrochemical stability entails evaluating the grand potential function Φ for all phases at a given applied Li chemical potential μ_{Li} and computing the grand potential convex hull. Phases on the convex hull of the grand potential function are thermodynamically electrochemically stable against the applied potential. Because electrodes operate by inserting or removing Li from the electrolyte, applying an electrode at a given potential (in volts vs Li/Li^+) is equivalent to applying a lithium chemical potential of the opposite sign (in electronvolts per atom). The grand potential function is computed as

$$\Phi = \frac{E - \mu_{\text{Li}} N_{\text{Li}}}{\sum_{i \neq \text{Li}} N_i} \quad (1)$$

where E is the standard formation enthalpy of the phase per formula unit, μ_{Li} is the (negative) applied chemical potential in electronvolts, N_{Li} is the number of Li atoms in the phase per formula unit, and $\sum_{i \neq \text{Li}} N_i$ is the number of non-Li atoms per formula unit. For simplicity, we assume that the entropic contribution to enthalpy is negligible and replace the enthalpy with the DFT-computed standard formation energy. A survey of experimental thermochemical data of over 30 solid sulfide materials³⁹ reveals that the contribution of entropic effects to the formation enthalpy at RT is typically around 2% and rarely higher than 7%. In diboron trisulfide (B_2S_3), the contribution is 1.9%. This suggests that neglecting to consider entropy may introduce an uncertainty on the order of tens of millielectronvolts per atom in our grand potential calculations.

We compute the grand potential function for all known stable crystalline phases of the Li–B–S system from Figure 2 over a range of applied potentials from 0 to 5 V versus Li/Li^+ . At each applied potential, we construct the convex hull by identifying the phases with the lowest grand potential function and then compute the energy above the convex hull of all phases. The predicted electrochemical stability window of an individual phase is given by the range of potentials for which the structure lies on the convex hull. In other words, a phase is predicted to be thermodynamically electrochemically stable at a given voltage if its grand potential function is more negative than the grand potential function of a linear combination of other phases, provided the other phases and their relative concentrations preserve the elemental ratios of the original phase.

In the thermodynamic picture, it is assumed that a phase will immediately decompose once it is no longer on the grand potential convex hull. In reality, the system will need to overcome an activation barrier for this reaction to proceed. The thermodynamic reduction and oxidation potentials are therefore typically upper and lower bounds, respectively, as the kinetics may stabilize the original phase at voltages outside of the thermodynamic electrochemical stability window.

Considering only the thermodynamics, we calculate the four fast-conducting Li–B–S phases to have the following electrochemical stability windows: 0.16 V for $\text{Li}_2\text{B}_2\text{S}_5$, 0.45 V for Li_3BS_3 , 0.50 V for $\text{Li}_5\text{B}_7\text{S}_{13}$, and 0.60 for $\text{Li}_9\text{B}_{19}\text{S}_{33}$. See the Methods section for computational details on the construction of the convex hull.

The predicted products resulting from oxidation on the cathode or reduction on the anode depend on the other stable phases present in the phase diagram and their computed grand potential function values. The presence of multiple stable superionic phases within the Li–B–S phase diagram suggests that superionic phases may break down into other superionic phases at certain applied voltages. If the products resulting from oxidation or reduction are other fast-conducting phases, the ionic impedance at the EEIs should remain low, and the effective electrochemical window of an electrolyte is widened.

In choosing the best Li–B–S electrolyte composition, it is therefore important to consider the products of redox chemistry at the electrode interfaces. The composition that maximizes both ionic conductivity and electrochemical stability may not necessarily be one of these four pure phases but may consist of a phase mixture of these phases. To this end, we examine the performance of phase mixtures of these fast-conducting structures over a range of compositions. Although we do not know a priori, a phase mixture electrolyte may exhibit ion conducting phases over a wider electrochemical range than the pure phases alone. We investigate the predicted interfacial chemistry of these compositions below.

Electrochemical Stability of the Li–B–S Mixture.

Using the methods described above, we predict the interfacial chemistry and therefore the effective electrochemical stability windows for all candidate compositions within the Li–B–S space. In a closed system, the Gibbs phase rule predicts that up to three phases can coexist in a ternary chemical space, but when a Li chemical potential is introduced, this decreases to two.⁴⁰ The 1–2 phases are predicted to be thermodynamically stable at a given potential, and their molar fractions depend on the ratio of boron to sulfur in the composition. In Figure 3, we provide the molar fraction of thermodynamically stable superionic phases as a function of applied potential and boron molar ratio, $B/(B + S)$. The optimal compositions are those for which the largest molar fraction of superionic phases is stable across the broadest voltage range.

The results of the analysis in Figure 3 show the remarkable result that a high concentration of superionic phases is predicted to be stable over a broad range of compositions and applied potentials in the Li–B–S space. This suggests that superionic mixtures of Li–B–S phases may be able to withstand a range of electrode potentials that would seek to induce redox reactions (variation along the x -axis in Figure 3), as well as a range of corrosive chemical conditions on the electrode that would change the composition with respect to B or S (variation along the y -axis in Figure 3). For example, a high concentration of superionic phases is predicted over a relatively wide range of potentials (1.59 to 2.19 V vs Li/Li^+) when the composition contains a B molar fraction of between 0.29 and 0.33; additionally, a high concentration of superionic phases is predicted to be present between 1.59 and 2.22 V versus Li/Li^+ between a B molar fraction of 0.37 and 0.4. The full list of the predicted 1–2 thermodynamically stable phases as a function of electrode potential and boron-to-sulfur ratio is provided in Table 1, with superionic phases in bold. Although the phases in Table 1 are predicted to form a stable mixture

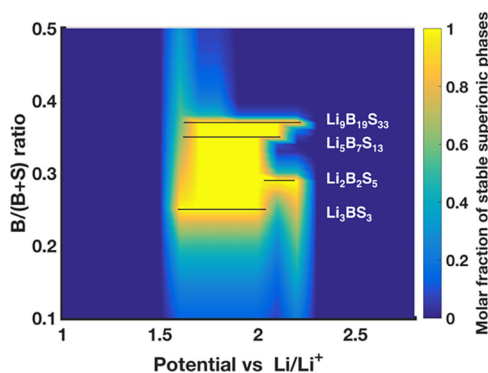


Figure 3. Superionic molar fraction vs composition and potential. The molar fraction of thermodynamically stable superionic phases is plotted as a function of the $B/(B + S)$ ratio and electrode potential. The optimal $B/(B + S)$ ratios are those which exhibit a high molar fraction of superionic phases over the widest potential range. No superionic phases are predicted to be thermodynamically stable below approximately 1.6 V or above 2.2 V vs Li/Li^+ , although high kinetic barriers may render them metastable. The $B/(B + S)$ values associated with the pure phases are denoted with horizontal black lines, and the width of the black lines indicates the pure phase electrochemical stability window. The highest molar fraction of superionic phases over the widest potential range occurs around a $B/(B + S)$ ratio of 0.365 (a B/S ratio of 1:1.74). This ratio corresponds to the $\text{Li}_9\text{B}_{19}\text{S}_{33}$ pure phase.

over the given potential ranges, our analysis does not consider the possible interfacial resistance between phases in the mixture.

The overall reactions provided in Table 1 consider only thermodynamic energy predictions and do not consider kinetic factors. The degree to which the diffusion kinetics affects the reaction rates at the solid–solid EEI is still largely an open question. All of the reactions predicted in Table 1 result in products with fundamentally different stoichiometries, thus requiring significant diffusion of Li, B, and S, possibly over the nanometer length scale or more. Although Li is predicted to be highly mobile, B and S are not. In fact, our DFT-MD simulations of all four superionic Li–B–S phases show zero migration of B or S in any of these phases over hundreds of picoseconds of high-temperature simulation, in contrast to the significant Li migration we observe. We would expect to see some B or S diffusion in these simulations if the energy barrier to long-range B or S diffusion was small enough for such diffusion to be facile. The absence of any B or S diffusion at all on these simulation timescales suggests that the diffusion barrier for B and S is significant, and we assume likely larger than 0.4 eV, an approximate upper bound ion conduction energy barrier in reasonably conductive materials. Thus, with B and S apparently quite immobile, it is possible that the fast ion conducting phases in the starting phase mixture will remain kinetically stabilized at voltages outside of the thermodynamic electrochemical stability windows. This will have the fortunate effect of widening the overall electrochemical stability window of the superionic phases.

As an example of this effect, consider the reaction trajectory for $\text{Li}_2\text{B}_2\text{S}_5$, where $B/(B + S) = 0.286$. The single-phase $\text{Li}_2\text{B}_2\text{S}_5$ is predicted to be thermodynamically electrochemically stable between electrode potentials of 2.03 and 2.19 V. As the electrode potential rises above 2.19 V, the predicted oxidation reaction is $\text{Li}_2\text{B}_2\text{S}_5 \rightleftharpoons 0.25\text{Li}_4 + 2\text{BS}_2 + 1.75\text{Li}$. Here, Li_4S_4 is a molecular solid that is predicted to be stable at high potentials

based on its computed grand potential function. As the potential falls below 2.03 V, the predicted reduction reaction is $\text{Li}_2\text{B}_2\text{S}_5 + 2\text{Li} \rightleftharpoons 1.125\text{Li}_3\text{BS}_3 + 0.125\text{Li}_5\text{B}_7\text{S}_{13}$, replacing one superionic conductor with two others. Below 1.62 V, the electrolyte is predicted to reduce further through the following reaction: $1.125\text{Li}_3\text{BS}_3 + 0.125\text{Li}_5\text{B}_7\text{S}_{13} + \text{Li} \rightleftharpoons 1.667\text{Li}_3\text{BS}_3 + 0.333\text{B}$. Below 1.59 V, the electrolyte is predicted to degrade further: $1.667\text{Li}_3\text{BS}_3 + 0.333\text{B} + 5\text{Li} \rightleftharpoons 5\text{Li}_2\text{S} + 2\text{B}$. Considering the whole reaction trajectory, at least one superionic Li–B–S phase is predicted to be stable across a window of 0.6 V, that is, between 1.59 and 2.19 V.

As the electrode potential decreases below 1.59 V or above 2.19 V, the grand potential of the superionic phases increases linearly with applied potential and they lift off the convex hull to be replaced by ionic insulators. If this degradation does occur, all fast ion conductors will give rise to slow ion conductors and battery operation will cease. However, if we assume that these reactants are kinetically stabilized until the grand potential difference between reactants and products exceeds the assumed B and S migration barriers of 0.4 eV/atom, lower reduction potentials and higher oxidation potentials may be reached before degradation. In Figure 4, we plot the grand potential energy above the hull as a function of applied potential for every phase. These calculations suggest that the superionic Li–B–S phases may tolerate potentials as low as approximately 1 V before kinetic barriers to reduction are overcome. Similarly, superionic Li–B–S phases may tolerate oxidation potentials as high as 4 V before oxidation is kinetically favored, with $\text{Li}_9\text{B}_{19}\text{S}_{33}$ appearing to be particularly stable at high potentials. This suggests that kinetic factors may widen the effective electrochemical stability window of superionic Li–B–S mixtures fivefold, from 0.6 to 3 V or more. For context, several known liquid electrolytes are stable in the 1–5 V range and beyond.^{34,41–43} An additional strategy for realizing a wider potential window if necessary might be to combine this electrolyte with degradation-resistant materials in a two- or three-electrolyte architecture.⁹

A key question for the cathodic stability of the Li–B–S system is which phase of elemental boron will form as Li_2S and elemental boron are predicted to form on the anode between 0.36 and 1.59 V regardless of the B molar ratio. The ground-state structure of elemental boron is a question that has received considerable attention in recent years.^{44–46} The PBE DFT calculations in the Materials Project database predict the ground state to be a semiconductor with a predicted band gap of 1.4 eV, but DFT also predicts metallic phases to be kinetically accessible by as little as ~ 0.1 eV per atom. It is also possible that metallic Li–B alloys will form on the anode below 1.59 V, analogous to the metallic Li–Ge alloys that have been reported to form on the lithium-metal anode in an LGPS battery.⁶ If metallic phases form, the electron insulating criteria outlined above will be violated and the interfacial products will not passivate the surface from further reaction.

At lower potentials (0–0.36 V), the thermodynamically favored products are Li_2S and metallic LiB.⁴⁷ Because LiB is metallic, it will also not passivate the anode from further reaction, suggesting that the Li–B–S electrolyte may be unsuitable for use in solid-state batteries with Li-metal anodes unless the superionic phases can be kinetically stabilized at these low potentials.

Currently, there are no other structures in the ICSD and MP databases in the relevant areas of the Li–B–S phase diagram, and we can find no other structures reported in the literature,

Table 1. Thermodynamic Reaction Pathways^a

reactions at electrode potentials as indicated above arrows, with superionic phases in bold;	
$x = \frac{1}{\xi} - 1$	
B molar ratio, $\xi = B/(B + S)$	
$0 \leq \xi \leq 0.25$	$x\text{Li}_2\text{S} + \text{LiB} \xrightarrow{0.36} x\text{Li}_2\text{S} + \text{B} \xrightarrow{1.59} \mathbf{Li}_3\text{BS}_3 + (x-3)\text{Li}_2\text{S}$ $\xrightarrow{2.04} 0.5\mathbf{Li}_2\text{B}_2\text{S}_5 + (x-2.5)\text{Li}_2\text{S} \xrightarrow{2.14} 0.5\mathbf{Li}_2\text{B}_2\text{S}_5 + (0.25x-0.63)\text{LiS}_4$ $\xrightarrow{2.19} (0.25x-0.5)\text{LiS}_4 + \text{BS}_2 \xrightarrow{3.76} (x-2)\text{S} + \text{BS}_2$
$0.25 \leq \xi \leq 0.286$	$x\text{Li}_2\text{S} + \text{LiB} \xrightarrow{0.36} x\text{Li}_2\text{S} + \text{B} \xrightarrow{1.59} 0.33x\mathbf{Li}_3\text{BS}_3 + (1-0.33x)\text{B}$ $\xrightarrow{1.62} (0.88x-1.63)\mathbf{Li}_3\text{BS}_3 + (0.38-0.13x)\mathbf{Li}_5\text{B}_7\text{S}_{13}$ $\xrightarrow{2.03} (2x-5)\mathbf{Li}_3\text{BS}_3 + (3-x)\mathbf{Li}_2\text{B}_2\text{S}_5 \xrightarrow{2.04} 0.5\mathbf{Li}_2\text{B}_2\text{S}_5$ $+ (x-2.5)\text{Li}_2\text{S} \xrightarrow{2.14} 0.5\mathbf{Li}_2\text{B}_2\text{S}_5 + (0.25x-0.63)\text{LiS}_4$ $\xrightarrow{2.19} (0.25x-0.5)\text{LiS}_4 + \text{BS}_2 \xrightarrow{3.76} (x-2)\text{S} + \text{BS}_2$
$0.286 \leq \xi \leq 0.333$	$x\text{Li}_2\text{S} + \text{LiB} \xrightarrow{0.36} x\text{Li}_2\text{S} + \text{B} \xrightarrow{1.59} 0.33x\mathbf{Li}_3\text{BS}_3 + (1-0.33x)\text{B}$ $\xrightarrow{1.62} (0.88x-1.63)\mathbf{Li}_3\text{BS}_3 + (0.38-0.13x)\mathbf{Li}_5\text{B}_7\text{S}_{13}$ $\xrightarrow{2.03} (0.78x-1.44)\mathbf{Li}_2\text{B}_2\text{S}_5 + (0.56-0.22x)\mathbf{Li}_5\text{B}_7\text{S}_{13}$ $\xrightarrow{2.07} (x-2)\mathbf{Li}_2\text{B}_2\text{S}_5 + (5-2x)\text{BS}_2 \xrightarrow{2.19} (0.25x-0.5)\text{LiS}_4 + \text{BS}_2$ $\xrightarrow{3.76} (x-2)\text{S} + \text{BS}_2$
$0.333 \leq \xi \leq 0.35$	$x\text{Li}_2\text{S} + \text{LiB} \xrightarrow{0.36} x\text{Li}_2\text{S} + \text{B} \xrightarrow{1.59} 0.33x\mathbf{Li}_3\text{BS}_3 + (1-0.33x)\text{B}$ $\xrightarrow{1.62} (0.88x-1.63)\mathbf{Li}_3\text{BS}_3 + (0.38-0.13x)\mathbf{Li}_5\text{B}_7\text{S}_{13}$ $\xrightarrow{2.03} (0.78x-1.44)\mathbf{Li}_2\text{B}_2\text{S}_5 + (0.56-0.22x)\mathbf{Li}_5\text{B}_7\text{S}_{13}$ $\xrightarrow{2.07} (2-x)\mathbf{Li}_5\text{B}_7\text{S}_{13} + (7x-13)\text{BS}_2 \xrightarrow{2.11} (0.4-0.2x)\mathbf{Li}_9\text{B}_{19}\text{S}_{33}$ $+ (3.8x-6.6)\text{BS}_2 \xrightarrow{2.22} (2-x)\text{B}_2\text{S}_3 + (2x-3)\text{BS}_2$
$0.35 \leq \xi \leq 0.365$	$x\text{Li}_2\text{S} + \text{LiB} \xrightarrow{0.36} x\text{Li}_2\text{S} + \text{B} \xrightarrow{1.59} 0.33x\mathbf{Li}_3\text{BS}_3 + (1-0.33x)\text{B}$ $\xrightarrow{1.62} 0.077x\mathbf{Li}_5\text{B}_7\text{S}_{13} + (1-0.54x)\text{B} \xrightarrow{1.62} (1.19x-2.06)\mathbf{Li}_5\text{B}_7\text{S}_{13}$ $+ (0.81-0.44x)\mathbf{Li}_9\text{B}_{19}\text{S}_{33} \xrightarrow{2.11} (0.4-0.2x)\mathbf{Li}_9\text{B}_{19}\text{S}_{33}$ $+ (3.8x-6.6)\text{BS}_2 \xrightarrow{2.22} (2-x)\text{B}_2\text{S}_3 + (2x-3)\text{BS}_2$
$0.365 \leq \xi \leq 0.4$	$x\text{Li}_2\text{S} + \text{LiB} \xrightarrow{0.36} x\text{Li}_2\text{S} + \text{B} \xrightarrow{1.59} 0.33x\mathbf{Li}_3\text{BS}_3 + (1-0.33x)\text{B}$ $\xrightarrow{1.62} 0.077x\mathbf{Li}_5\text{B}_7\text{S}_{13} + (1-0.54x)\text{B} \xrightarrow{1.62} 0.03\mathbf{Li}_9\text{B}_{19}\text{S}_{33}$ $+ (1-0.58x)\text{B} \xrightarrow{1.87} (0.22x-0.33)\mathbf{Li}_9\text{B}_{19}\text{S}_{33} + (3.67-2.11x)\text{B}_2\text{S}_3$ $\xrightarrow{2.22} (2-x)\text{B}_2\text{S}_3 + (2x-3)\text{BS}_2$
$0.4 \leq \xi \leq 1$	$x\text{Li}_2\text{S} + \text{LiB} \xrightarrow{0.36} x\text{Li}_2\text{S} + \text{B} \xrightarrow{1.59} 0.33x\mathbf{Li}_3\text{BS}_3 + (1-0.33x)\text{B}$ $\xrightarrow{1.62} 0.077x\mathbf{Li}_5\text{B}_7\text{S}_{13} + (1-0.54x)\text{B} \xrightarrow{1.62} 0.03\mathbf{Li}_9\text{B}_{19}\text{S}_{33}$ $+ (1-0.58x)\text{B} \xrightarrow{1.87} 0.33\text{B}_2\text{S}_3 + (1-0.67x)\text{B}$

^aWe provide the overall reaction for the Li–B–S electrolyte system as calculated with DFT grand potential methods as a function of the $B/(B + S)$ molar ratio, ξ , which runs from 0 (only Li and S) to 1 (only Li and B). The electrochemical potential (vs Li/Li⁺) at which each reaction is predicted to occur is provided above the reaction arrows in the order of increasing potential. The products on the far left of each set of reactions are predicted to be stable against Li metal (0 V), while the products on the far right are predicted to be stable against any potential above the potential listed over the furthest-right arrow. Superionic phases are denoted in bold.

but the discovery and/or inclusion of new phases may alter the result of the calculations here. The accuracy of these electrochemical predictions is subject to the accuracy of the DFT energy calculations and the thermodynamic assumptions employed here, as well as the completeness of the structures in the phase diagram. This analysis also does not consider the chemical stability of the Li–B–S phases with respect to electrode materials. The degree of chemical stability depends on the choice of electrodes, and chemical reactivity may

produce different decomposition products on the EEs rather than the products of electrochemical reactivity.

Energy Density and Cost. Energy density and cost are important practical considerations for any new battery material and should be incorporated into the materials discovery process. This is especially true for candidate SSLIB chemistries because there must be potential for significant improvement over the incumbent liquid electrolyte technology to become commercially attractive. In order to improve gravimetric

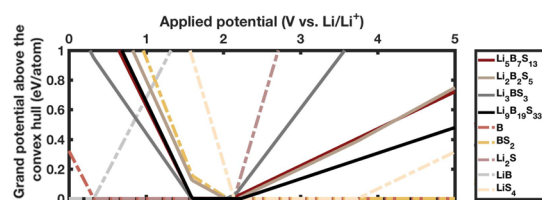


Figure 4. Analysis of electrochemical stability. We compute the thermodynamic electrochemical stability windows for all stable phases in the Li–B–S system using PBE DFT. Single phases are predicted to be thermodynamically electrochemically stable over the range of applied voltages for which they lie on the grand potential function convex hull. The thermodynamic electrochemical stability windows of the four superionic Li–B–S phases all lie between 1.59 and 2.22 V vs Li/Li⁺. Outside of this voltage range, the difference between the single-phase grand potential and the convex hull grows linearly. Although the kinetics behind the various Li–B–S degradation reactions is not known, we assume that the reactions may be stabilized until the grand potential above the convex hull of the Li–B–S phases exceeds 0.4 eV/atom. Our calculations suggest that Li₃B₇S₃ may be the most stable against reduction of all four superionic Li–B–S phases, possibly remaining kinetically stabilized against anode potentials as low as 1 V. Li₉B₁₉S₃₃ appears to be the most stable against oxidation and may remain stabilized against cathode potentials as high as 4.5 V.

energy density, solid electrolyte materials should be made of low-mass elements. In this respect, lithium, boron, and sulfur are favorable elements. The densities of Li₃B₇S₃, Li₃B₇S₁₃, Li₂B₂S₅, and Li₉B₁₉S₃₃ are 1.65, 2.06, 1.77, and 2.18 g cm⁻³, respectively. This is a factor of 2 less dense than Li_{0.5}La_{0.5}TiO₃ (LLTO, 4.68 g cm⁻³) and Li₇La₃Zr₂O₁₂ (LLZO, 4.99 g cm⁻³) and similar to that of LGPS (1.98 g cm⁻³).

At the time of publication, the price to purchase elemental Li, B, and S in large industrial quantities is approximately \$20 per kg, \$5 per kg, and \$1 per kg, respectively. At this price point, the raw materials cost of a Li–B–S solid electrolyte will be ~0.05 USD/m² per 10 μm of thickness. A recent analysis by Li et al. proposed that the low cost of S and its high earth abundance make sulfur-based cathodes one of the few cost-competitive routes for electrochemical energy storage compared to the incumbent technology on a capacity per dollar metric;⁴⁸ sulfur-based solid electrolytes are desirable for the same reasons. Additionally, Li–B–S is free of germanium (~\$500 per kg), making the raw materials significantly cheaper than those in LGPS. Manufacturing will bring additional costs, and the magnitude of these costs will vary depending on the economics and scalability of the synthesis routes. Regardless, the cost of the raw materials suggests that Li–B–S is a strong candidate for commercial manufacture at a cost below McCloskey's threshold of 10 USD/m² for lithium-ion electrolytes.⁴⁹ This cost target has since been adopted by the US Department of Energy's Advanced Research Projects Agency-Energy (ARPA-E).⁵⁰

CONCLUSIONS

The identification of solid lithium-ion conductors that oxidize and reduce into nonmetallic ion conducting products at the electrolyte–electrode interface would be a significant advancement toward realizing an SSLIB with superior energy density to traditional lithium-ion batteries. To this end, we computationally investigate the electrolyte performance of the Li–B–S chemical system. We predict that four structures in the Li–B–S system will exhibit a superionic ionic conductivity (10⁻¹ to

10⁻⁶ S cm⁻¹) at RT over a range of applied Li potentials. Thermodynamic and kinetic considerations suggest that fast lithium-ion conductors may form or persist on the EEIs during electrolytic oxidation and reduction by the electrodes. Li–B–S phase mixtures are generally predicted to be effectively thermodynamically stable in a window of 1.6–2.2 V versus Li/Li⁺, a voltage range twice that of LGPS, and may be kinetically stabilized over the 1.0–4.0 V range and beyond. In Figure 5, we plot the performance characteristics of known Li-

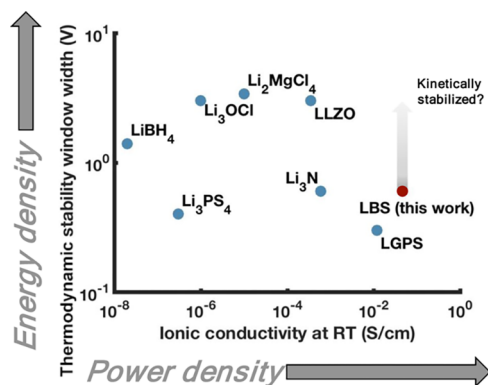


Figure 5. Solid electrolyte performance characteristics. Here, we provide the thermodynamic electrochemical stability window widths computed with PBE DFT^{5,37,38} and the experimentally reported ionic conductivities^{4,60–65} (on a log–log scale) of several known solid Li-ion conductors, including the predicted values for the best Li–B–S electrolyte compositions reported here. An overall ionic conductivity of 46 mS cm⁻¹ in Li–B–S is computed by taking the weighted mean of the bulk ionic conductivities of Li₃B₇S₁₃, Li₂B₂S₅, Li₃B₇S₃, and Li₉B₁₉S₃₃, where the weights are proportional to the thermodynamic electrochemical stability window widths of the phases. Taking the ionic conductivity as an indicator of power density and the electrochemical stability as an indicator of energy density, we predict that Li–B–S enables twice the energy density of LGPS and 3 times the power density. By comparison, LLZO exhibits a stability window 5 times wider than that of Li–B–S but an ionic conductivity value over 100 times lower.

ion conductors and the characteristics of the Li–B–S system we predict here. Taking ionic conductivity as an indicator of power density and electrochemical stability window as an indicator of energy density, this plot shows that Li–B–S may offer an increase in both energy density and power density over LGPS.

More generally, this approach may be applied beyond the Li–B–S system. Narrow electrochemical stability in fast ion conducting materials is a persistent issue. In this work, we explore a new approach to enhancing electrochemical stability by combining fast ion conducting phases from the same chemical family. This approach could be extended to other solid electrolyte systems where multiple fast ion conducting phases exist and electrochemical stability is a concern.

Our study indicates that solid Li–B–S electrolytes may offer comparable or significantly improved performance over the best existing solid electrolytes in terms of ionic conductivity, electrochemical stability, materials cost, and weight. Synthesis routes for Li₃B₇S₁₃ and Li₉B₁₉S₃₃ have been reported.¹⁸ We welcome further computational and experimental investigations to assess the feasibility of synthesis as well as the long-term performance and stability of solid Li–B–S electrolytes.

METHODS

DFT Molecular Dynamics Simulation. For the simulation of DFT-MD in $\text{Li}_5\text{B}_7\text{S}_{13}$, $\text{Li}_2\text{B}_2\text{S}_5$, Li_3BS_3 , and $\text{Li}_9\text{B}_{19}\text{S}_{33}$, we utilize the Vienna ab initio simulation package (VASP)⁵¹ with the GGA of PBE²⁷ and the PAW method.²⁸ Our simulations use the NVT canonical ensemble. The unit cells for $\text{Li}_5\text{B}_7\text{S}_{13}$, $\text{Li}_2\text{B}_2\text{S}_5$, and Li_3BS_3 are obtained from the Materials Project database.⁵² We confirm that the structures for $\text{Li}_2\text{B}_2\text{S}_5$ and Li_3BS_3 are the same as those originally reported in the literature, while the symmetry of $\text{Li}_5\text{B}_7\text{S}_{13}$ (space group Cc) is slightly different from that originally reported (space group C2/c).¹⁸ The unit cell for $\text{Li}_9\text{B}_{19}\text{S}_{33}$ is obtained from experimental reports¹⁸ via the Inorganic Crystal Structure Database, and a lattice relaxation was performed before initiating DFT-MD. We simulate supercells of 99, 71, 111, and 244 atoms, respectively. The large unit cell for $\text{Li}_9\text{B}_{19}\text{S}_{33}$ caused DFT-MD simulations to run extremely slowly, so we ran two separate DFT-MD simulations in order to generate sufficient diffusivity data, rather than one long simulation. One lithium vacancy is introduced per unit cell. We use the Li_{-sv} , B, and S pseudopotentials, a plane wave cutoff energy of 499 eV for all structures, and a gamma-point only k -mesh. This corresponds to a reciprocal lattice k -point density of 0.59, 0.68, 0.48, and 0.25 nm^{-3} . The VASP input files are generated using the `pymatgen.io.vasp.sets` module of Pymatgen.^{53,54}

Ionic Conductivity Calculation. To compute the ionic conductivity from DFT-MD, we first compute the three-dimensional lithium diffusivity as a function of temperature $D(T)$, that is, the average of the diagonal entries of the diffusivity tensor, and then calculate the ionic conductivity through the Einstein relation. We compute $D(T)$ from one-sixth of the slope of the mean-squared displacement (MSD) of all Li over time at a given simulation temperature, $\text{MSD}(T, t) = \frac{1}{N_{\text{Li}}} \sum_{i=1}^{N_{\text{Li}}} [r_i(T, t) - r_i(T, 0)]^2$. The squared displacement is averaged over all N_{Li} Li atoms in the simulation.

$$D(T) = \frac{1}{6} \frac{\Delta \text{MSD}}{\Delta t} \quad (2)$$

There are natural thermal fluctuations of the MSD curves, which may be exacerbated by the shorter simulation times employed here. We take the slope of the MSD curve as the median slope when considering all time origins up to 75% of the total simulation time in 100 equally spaced intervals. We compute the uncertainty of the diffusivities as the 25th and 75th percentiles of these distributions of slope values.

Plots of the simulated Li MSD versus time curves for all four materials at all simulation temperatures are provided in Figure S1 of the Supporting Information. Additionally, we plot the MSD of the sublattice and confirm that none of the materials melt during the simulations. The displacement of the center of mass of Li was recorded throughout the simulations, and we confirmed that there was no significant movement of the Li center of mass in any materials at any temperature.

The diffusivities and uncertainties are calculated at 900, 700, 400, and 293 K. The RT diffusivities are converted to ionic conductivities using the Einstein relation

$$\sigma(T) = \frac{D(T)nq^2}{k_{\text{B}}T} \quad (3)$$

where n is the Li-ion number density and q is the average effective charge on the Li ions. We compute the average charge on Li using the converged electron densities computed from DFT and the Bader charge analysis methods of Henkelman et al.^{55–58} In these DFT calculations, we use a plane wave cutoff of 520 eV and a Monkhorst–Pack k -point mesh with a density of at least 1000 per atom. We compute the Bader charge on $\text{Li}_5\text{B}_7\text{S}_{13}$, $\text{Li}_2\text{B}_2\text{S}_5$, and Li_3BS_3 to be 0.89, 0.90, and 0.88, respectively.

Low-temperature simulations often do not provide sufficient statistics to make a converged prediction of diffusivity, so we assume the Arrhenius dynamics to extrapolate the high-temperature

diffusivities to RT. In all cases, the simulations at 293 K are taken to be not converged, while the convergence at 400 K is clear for $\text{Li}_5\text{B}_7\text{S}_{13}$ but questionable for the other three phases. We note the work of He et al.³⁰ that suggests considering diffusivities to be converged when the total Li MSD is on the order of 100 \AA^2 , which rules out all 400 K simulations except that of $\text{Li}_5\text{B}_7\text{S}_{13}$. We compute the RT ionic conductivity with the 400 K results included in the extrapolation and without them. Figure 1 shows all computed conductivities, but the dotted extrapolation lines are fit only to the 900, 700, and 400 K data for $\text{Li}_5\text{B}_7\text{S}_{13}$ and the 900 and 700 K data for all other phases. We note that the 400 K data for $\text{Li}_9\text{B}_{19}\text{S}_{33}$ and the 293 K data for $\text{Li}_5\text{B}_7\text{S}_{13}$ align closely to the extrapolation. For the other two phases, the simulated low-temperature conductivities are significantly higher than the extrapolations.

To compute the uncertainties associated with the extrapolation of conductivity to RT, we fit a simple linear model along the upper and lower limits of the error bars (on a log scale) versus inverse temperature for each composition. The predicted error bar width at inverse RT is assumed to be the difference in these two linear extrapolations at RT.

To confirm convergence in Li ionic conductivity with respect to unit cell size and Li vacancy concentration, we simulate DFT-MD in all three phases at 900 K with doubled unit cells and zero Li vacancy concentration. For $\text{Li}_5\text{B}_7\text{S}_{13}$ and Li_3BS_3 , we find very close alignment between the Li diffusivity of these simulations with the original simulations: 0.88 versus 1.0 $\text{\AA}^2 \text{ps}^{-1}$ for $\text{Li}_5\text{B}_7\text{S}_{13}$ and 0.55 versus 0.61 $\text{\AA}^2 \text{ps}^{-1}$ for Li_3BS_3 . For $\text{Li}_2\text{B}_2\text{S}_5$, the doubled unit cell with zero Li vacancy concentration showed no Li diffusivity after 33 ps of simulation. We do not perform this analysis for $\text{Li}_9\text{B}_{19}\text{S}_{33}$, given the large unit cell size.

Convex Hull Calculation. To calculate the electrochemical stability windows provided in Figure 3 and Table 1, we compute the grand potential $\Phi(\mu_{\text{Li}})$ of all phases at a range of applied Li chemical potentials $0 \leq \mu_{\text{Li}} \leq 5 \text{ V}$ versus Li/Li⁺ and construct the convex hull. The convex hull represents the lowest grand potential that can be accessed at a given composition, and this defines the thermodynamically stable phase(s).

For a grand potential phase diagram at a given chemical potential, we employ a modified Graham scan algorithm⁵⁹ for drawing the convex hull. Beginning with the lowest grand potential end member on the left-hand side of the diagram, phase i , we compute the angle θ_{ij} from the horizontal formed when drawing a line from this phase to all other phases j . Defining θ_{ij} as zero along the positive y -axis and increasing counterclockwise, we search for phase j^* that forms an angle closest to π , provided that $\pi < \theta_{ij} < 2\pi$ (i.e., j^* is down and to the right). This phase j^* is identified as sitting on the convex hull, and a line is drawn between the two phases. For any phases k existing above the convex hull between phases i and j^* , the energy above the hull is computed as the grand potential difference between this line and the grand potential of phase k . The same procedure is then repeated, with the search now spreading out from the new phase j^* . This is repeated until the search identifies the lowest potential end member on the right-hand side of the phase diagram.

Ternary Phase Diagram. The ternary Li–B–S phase diagram shown in Figure 2 is calculated using the `pymatgen.analysis.phase_diagram` module of `pymatgen`.^{37,38}

ASSOCIATED CONTENT

Supporting Information

The Supporting Information is available free of charge at <https://pubs.acs.org/doi/10.1021/acsami.9b19091>.

MSD data from DFT-MD for $\text{Li}_5\text{B}_7\text{S}_{13}$, Li_3BS_3 , $\text{Li}_2\text{B}_2\text{S}_5$, and $\text{Li}_9\text{B}_{19}\text{S}_{33}$ at 900, 700, 400, and 293 K (PDF)

AUTHOR INFORMATION

Corresponding Author

Evan J. Reed – Department of Materials Science & Engineering, Stanford University, Stanford, California 94305, United States; Email: evanreed@stanford.edu

Authors

Austin D. Sendek – Department of Applied Physics and Department of Materials Science & Engineering, Stanford University, Stanford, California 94305, United States; Aionics, Inc., Evanston, Wyoming 82930, United States

Evan R. Antoniuk – Department of Chemistry, Stanford University, Stanford, California 94305, United States; orcid.org/0000-0003-3338-1615

Ekin D. Cubuk – Google Brain, Mountain View, California 94043, United States; orcid.org/0000-0002-4273-1974

Brandi Ransom – Department of Materials Science & Engineering, Stanford University, Stanford, California 94305, United States; orcid.org/0000-0002-9041-6725

Brian E. Francisco – Solid Power, Inc., Louisville, Colorado 80027, United States

Josh Buettner-Garrett – Solid Power, Inc., Louisville, Colorado 80027, United States

Yi Cui – Department of Materials Science & Engineering, Stanford University, Stanford, California 94305, United States; orcid.org/0000-0002-6103-6352

Complete contact information is available at: <https://pubs.acs.org/10.1021/acsami.9b19091>

Notes

The authors declare no competing financial interest.

ACKNOWLEDGMENTS

The authors acknowledge funding from the TomKat Center for Sustainable Energy at Stanford University and the Toyota Research Institute Accelerated Materials Design and Discovery program. The authors acknowledge helpful discussions with Nadia Ahlborg, Dr. Jin Xie, Dr. Chenxi Zu, and Dr. Xiaokun Zhang.

REFERENCES

- (1) Janek, J.; Zeier, W. G. A Solid Future for Battery Development. *Nat. Energy* **2016**, *1*, 16141.
- (2) Manthiram, A.; Yu, X.; Wang, S. Lithium Battery Chemistries Enabled by Solid-State Electrolytes. *Nat. Rev. Mater.* **2017**, *2*, 16103.
- (3) Koerver, R.; Aygün, I.; Leichtweiß, T.; Dietrich, C.; Zhang, W.; Binder, J. O.; Hartmann, P.; Zeier, W. G.; Janek, J. Capacity Fade in Solid-State Batteries: Interphase Formation and Chemomechanical Processes in Nickel-Rich Layered Oxide Cathodes and Lithium Thiophosphate Solid Electrolytes. *Chem. Mater.* **2017**, *29*, 5574–5582.
- (4) Kamaya, N.; Homma, K.; Yamakawa, Y.; Hirayama, M.; Kanno, R.; Yonemura, M.; Kamiyama, T.; Kato, Y.; Hama, S.; Kawamoto, K.; Mitsui, A. A Lithium Superionic Conductor. *Nat. Mater.* **2011**, *10*, 682–686.
- (5) Richards, W. D.; Miara, L. J.; Wang, Y.; Kim, J. C.; Ceder, G. Interface Stability in Solid-State Batteries. *Chem. Mater.* **2016**, *28*, 266–273.
- (6) Wenzel, S.; Randau, S.; Leichtweiß, T.; Weber, D. A.; Sann, J.; Zeier, W. G.; Janek, J. Direct Observation of the Interfacial Instability of the Fast Ionic Conductor Li₁₀GeP₂S₁₂ at the Lithium Metal Anode. *Chem. Mater.* **2016**, *28*, 2400–2407.
- (7) Whittingham, M. S. Lithium Batteries and Cathode Materials. *Chem. Rev.* **2004**, *104*, 4271–4302.

(8) Yamaki, J.-i.; Egashira, M.; Okada, S. Potential and Thermodynamics of Graphite Anodes in Li-Ion Cells. *J. Electrochem. Soc.* **2000**, *147*, 460–465.

(9) Sendek, A. D.; Cheon, G.; Pasta, M.; Reed, E. J. Quantifying the Search for Solid Li-Ion Electrolyte Materials by Anion: A Data-Driven Perspective. *J. Phys. Chem. C* **2020**, *124*, 8067–8079.

(10) Muy, S.; Bachman, J. C.; Giordano, L.; Chang, H.-H.; Abernathy, D. L.; Bansal, D.; Delaire, O.; Hori, S.; Kanno, R.; Maglia, F.; Lupart, S.; Lamp, P.; Shao-Horn, Y. Tuning Mobility and Stability of Lithium Ion Conductors Based on Lattice Dynamics. *Energy Environ. Sci.* **2018**, *11*, 850–859.

(11) Levasseur, A.; Olazcuaga, R.; Kbal, M.; Zahir, M.; Hagenmuller, P. Synthesis and Electrical Properties of New Sulfide Glasses with High Ionic Conductivity. *C. R. Seances Acad. Sci., Ser. 2* **1981**, *293*, 563–565.

(12) Wada, H.; Menetrier, M.; Levasseur, A.; Hagenmuller, P. Preparation and Ionic Conductivity of New B₂S₃-Li₂S-LiI Glasses. *Mater. Res. Bull.* **1983**, *18*, 189–193.

(13) Takada, K.; Inada, T.; Kajiyama, A.; Kouguchi, M.; Sasaki, H.; Kondo, S.; Michiue, Y.; Nakano, S.; Tabuchi, M.; Watanabe, M. Solid State Batteries with Sulfide-Based Solid Electrolytes. *Solid State Ionics* **2004**, *172*, 25–30.

(14) Knauth, P. Inorganic Solid Li Ion Conductors: An Overview. *Solid State Ionics* **2009**, *180*, 911–916.

(15) Conrad, O.; Jansen, C.; Krebs, B. Bor-Schwefel- und Bor-Selen-Verbindungen – von Prinzipien einzigartiger Molekülstrukturen zu neuartigen Polymermaterialien. *Angew. Chem.* **1998**, *110*, 3396–3407.

(16) Grüne, M.; Müller-Warmuth, W.; zum Hebel, P.; Krebs, B. Unusual Lithium Dynamics and NMR Relaxation in a Novel Crystalline Thioborate-Sulfide. *Solid State Ionics* **1993**, *66*, 165–173.

(17) Zum Hebel, P.; Krebs, B.; Grüne, M.; Müller-Warmuth, W. Preparation, crystal structure and ⁷Li NMR of Li_{6+2x}[B₁₀S₁₈]S_x (x ≈ 1). *Solid State Ionics* **1990**, *43*, 133–142.

(18) Hiltmann, F.; Zum Hebel, P.; Hammerschmidt, A.; Krebs, B. Li₅B₇S₁₃ und Li₉B₁₉S₃₃: Zwei Lithiumthioborate Mit Neuen Hochpolymeren Anionengerüsten. *Z. Anorg. Allg. Chem.* **1993**, *619*, 293–302.

(19) Jansen, C.; Küper, J. r.; Krebs, B. Na₂B₂S₅ and Li₂B₂S₅: Two Novel Perthioborates with Planar 1,2,4-Trithia-3,5-Diborolane Rings. *Z. Für Anorg. Allg. Chem.* **1995**, *621*, 1322.

(20) Vinatier, P.; Menetrier, M.; Levasseur, A. Structure and Ionic Conduction in Lithium Thioborate Glasses and Crystals. *Phys. Chem. Glas.* **2003**, *44*, 135–142.

(21) Persson, K. *Materials Data on Li₃B₇S₁₃ (SG:9) by Materials Project*, 2014.

(22) Persson, K. *Materials Data on Li₂B₂S₅ (SG:63) by Materials Project*, 2016.

(23) Persson, K. *Materials Data on Li₃BS₃ (SG:62) by Materials Project*, 2014.

(24) Hiltmann, F.; Jansen, C.; Krebs, B. Li₃BS₃ und LiSrBS₃: Neue Orthothioborate mit trigonal-planar koordiniertem Bor. *Z. Für Anorg. Allg. Chem.* **1996**, *622*, 1508–1514.

(25) Sendek, A. D.; Yang, Q.; Cubuk, E. D.; Duerloo, Y.; Cui, Y.; Reed, E. J. Holistic Computational Structure Screening of More than 12000 Candidates for Solid Lithium-Ion Conductor Materials. *Energy Environ. Sci.* **2017**, *10*, 306–320.

(26) Sendek, A. D.; Cubuk, E. D.; Antoniuk, E. R.; Cheon, G.; Cui, Y.; Reed, E. J. Machine Learning-Assisted Discovery of Solid Li-Ion Conducting Materials. *Chem. Mater.* **2019**, *31*, 342–352.

(27) Perdew, J. P.; Burke, K.; Ernzerhof, M. Generalized Gradient Approximation Made Simple. *Phys. Rev. Lett.* **1996**, *77*, 3865–3868.

(28) Blöchl, P. E. Projector Augmented-Wave Method. *Phys. Rev. B: Condens. Matter Phys.* **1994**, *50*, 17953–17979.

(29) Mo, Y.; Ong, S. P.; Ceder, G. First Principles Study of the Li₁₀GeP₂S₁₂ Lithium Super Ionic Conductor Material. *Chem. Mater.* **2012**, *24*, 15–17.

(30) He, X.; Zhu, Y.; Epstein, A.; Mo, Y. Statistical Variances of Diffusional Properties from Ab Initio Molecular Dynamics Simulations. *Npj Comput. Mater.* **2018**, *4*, 18.

- (31) Chan, M. K. Y.; Ceder, G. Efficient Band Gap Prediction for Solids. *Phys. Rev. Lett.* **2010**, *105*, 196403.
- (32) Heyd, J.; Scuseria, G. E.; Ernzerhof, M. Hybrid Functionals Based on a Screened Coulomb Potential. *J. Chem. Phys.* **2003**, *118*, 8207–8215.
- (33) Ong, S. P.; Mo, Y.; Richards, W. D.; Miara, L.; Lee, H. S.; Ceder, G. Phase Stability, Electrochemical Stability and Ionic Conductivity of the $\text{Li}_{10\pm 1}\text{MP}_2\text{X}_{12}$ (M = Ge, Si, Sn, Al or P, and X = O, S or Se) Family of Superionic Conductors. *Energy Environ. Sci.* **2013**, *6*, 148–156.
- (34) Ong, S. P.; Andreussi, O.; Wu, Y.; Marzari, N.; Ceder, G. Electrochemical Windows of Room-Temperature Ionic Liquids from Molecular Dynamics and Density Functional Theory Calculations. *Chem. Mater.* **2011**, *23*, 2979–2986.
- (35) Curtarolo, S.; Setyawan, W.; Hart, G. L. W.; Jahnatek, M.; Chepulskii, R. V.; Taylor, R. H.; Wang, S.; Xue, J.; Yang, K.; Levy, O.; Mehl, M. J.; Stokes, H. T.; Demchenko, D. O.; Morgan, D. AFLOW: An Automatic Framework for High-Throughput Materials Discovery. *Comput. Mater. Sci.* **2012**, *58*, 218–226.
- (36) Setyawan, W.; Curtarolo, S. High-Throughput Electronic Band Structure Calculations: Challenges and Tools. *Comput. Mater. Sci.* **2010**, *49*, 299–312.
- (37) Ong, S. P.; Jain, A.; Hautier, G.; Kang, B.; Ceder, G. Thermal Stabilities of Delithiated Olivine MPO_4 (M = Fe, Mn) Cathodes Investigated Using First Principles Calculations. *Electrochem. Commun.* **2010**, *12*, 427–430.
- (38) Ong, S. P.; Wang, L.; Kang, B.; Ceder, G. Li–Fe–P–O₂ Phase Diagram from First Principles Calculations. *Chem. Mater.* **2008**, *20*, 1798–1807.
- (39) Barin, I. *Thermochemical Data of Pure Substances*, 3rd ed.; Wiley, 2008.
- (40) Gibbs, J. W. On the Equilibrium of Heterogenous Substances. *Transactions of the Connecticut Academy of Arts and Sciences*; 1874–1878, Vol. 3, pp 108–248, 343–524.
- (41) Li, Q.; Chen, J.; Fan, L.; Kong, X.; Lu, Y. Progress in Electrolytes for Rechargeable Li-Based Batteries and beyond. *Green Energy Environ* **2016**, *1*, 18–42.
- (42) Qu, X.; Jain, A.; Rajput, N. N.; Cheng, L.; Zhang, Y.; Ong, S. P.; Brafman, M.; Maginn, E.; Curtiss, L. A.; Persson, K. A. The Electrolyte Genome Project: A Big Data Approach in Battery Materials Discovery. *Comput. Mater. Sci.* **2015**, *103*, 56–67.
- (43) DiLeo, R. A.; Marschilok, A. C.; Takeuchi, K. J.; Takeuchi, E. S. Battery Electrolytes Based on Unsaturated Ring Ionic Liquids: Conductivity and Electrochemical Stability. *J. Electrochem. Soc.* **2013**, *160*, A1399–A1405.
- (44) An, Q.; Reddy, K. M.; Xie, K. Y.; Hemker, K. J.; Goddard, W. A. New Ground-State Crystal Structure of Elemental Boron. *Phys. Rev. Lett.* **2016**, *117*, 085501.
- (45) Ogitsu, T.; Schwegler, E.; Galli, G. β -Rhombohedral Boron: At the Crossroads of the Chemistry of Boron and the Physics of Frustration. *Chem. Rev.* **2013**, *113*, 3425.
- (46) White, M. A.; Cerqueira, A. B.; Whitman, C. A.; Johnson, M. B.; Ogitsu, T. Determination of Phase Stability of Elemental Boron. *Angew. Chem., Int. Ed.* **2015**, *54*, 3626–3629.
- (47) Persson, K. *Materials Data on LiB (SG:194) by Materials Project*; LBNL Materials Project; Lawrence Berkeley National Laboratory (LBNL): Berkeley, CA (United States), 2016.
- (48) Li, Z.; Pan, M. S.; Su, L.; Tsai, P.-C.; Badel, A. F.; Valle, J. M.; Eiler, S. L.; Xiang, K.; Brushett, F. R.; Chiang, Y.-M. Air-Breathing Aqueous Sulfur Flow Battery for Ultralow-Cost Long-Duration Electrical Storage. *Joule* **2017**, *1*, 306–327.
- (49) McCloskey, B. D. Attainable Gravimetric and Volumetric Energy Density of Li–S and Li Ion Battery Cells with Solid Separator-Protected Li Metal Anodes. *J. Phys. Chem. Lett.* **2015**, *6*, 4581–4588.
- (50) *Integration and Optimization of Novel Ion Conducting Solids (IONICS)*; Funding Opportunity Announcement; ARPA-E, 2016.
- (51) Kresse, G.; Furthmüller, J. Efficient iterative schemes for ab initio total-energy calculations using a plane-wave basis set. *Phys. Rev. B: Condens. Matter Mater. Phys.* **1996**, *54*, 11169–11186.
- (52) Jain, A.; Ong, S. P.; Hautier, G.; Chen, W.; Richards, W. D.; Dacek, S.; Cholia, S.; Gunter, D.; Skinner, D.; Ceder, G.; Persson, K. A. Commentary: The Materials Project: A Materials Genome Approach to Accelerating Materials Innovation. *APL Mater.* **2013**, *1*, 011002.
- (53) Ong, S. P.; Richards, W. D.; Jain, A.; Hautier, G.; Kocher, M.; Cholia, S.; Gunter, D.; Chevrier, V. L.; Persson, K. A.; Ceder, G. Python Materials Genomics (Pymatgen): A Robust, Open-Source Python Library for Materials Analysis. *Comput. Mater. Sci.* **2013**, *68*, 314–319.
- (54) Jain, A.; Hautier, G.; Moore, C. J.; Ping Ong, S.; Fischer, C. C.; Mueller, T.; Persson, K. A.; Ceder, G. A High-Throughput Infrastructure for Density Functional Theory Calculations. *Comput. Mater. Sci.* **2011**, *50*, 2295–2310.
- (55) Henkelman, G.; Arnaldsson, A.; Jónsson, H. A Fast and Robust Algorithm for Bader Decomposition of Charge Density. *Comput. Mater. Sci.* **2006**, *36*, 354–360.
- (56) Sanville, E.; Kenny, S. D.; Smith, R.; Henkelman, G. Improved Grid-Based Algorithm for Bader Charge Allocation. *J. Comput. Chem.* **2007**, *28*, 899–908.
- (57) Tang, W.; Sanville, E.; Henkelman, G. A Grid-Based Bader Analysis Algorithm without Lattice Bias. *J. Phys.: Condens. Matter* **2009**, *21*, 084204.
- (58) Yu, M.; Trinkle, D. R. Accurate and Efficient Algorithm for Bader Charge Integration. *J. Chem. Phys.* **2011**, *134*, 064111.
- (59) Graham, R. L. An efficient algorithm for determining the convex hull of a finite planar set. *Set. Inf. Process. Lett.* **1972**, *1*, 132–133.
- (60) Matsuo, M.; Remhof, A.; Martelli, P.; Caputo, R.; Ernst, M.; Miura, Y.; Sato, T.; Oguchi, H.; Maekawa, H.; Takamura, H.; Borgschulte, A.; Züttel, A.; Orimo, S.-i. Complex Hydrides with (BH₄)⁻ and (NH₂)⁻ Anions as New Lithium Fast-Ion Conductors. *J. Am. Chem. Soc.* **2009**, *131*, 16389–16391.
- (61) Tachez, M.; Malugani, J.; Mercier, R.; Robert, G. Ionic Conductivity of and Phase Transition in Lithium Thiophosphate Li₃PS₄. *Solid State Ionics* **1984**, *14*, 181–185.
- (62) Zhao, Y.; Daemen, L. L. Superionic Conductivity in Lithium-Rich Anti-Perovskites. *J. Am. Chem. Soc.* **2012**, *134*, 15042–15047.
- (63) Kanno, R.; Takeda, Y.; Yamamoto, O. Ionic Conductivity of Solid Lithium Ion Conductors with the Spinel Structure: Li₂MCl₄ (M = Mg, Mn, Fe, Cd). *Mater. Res. Bull.* **1981**, *16*, 999–1005.
- (64) Li, W.; Wu, G.; Araújo, C. M.; Scheicher, R. H.; Blomqvist, A.; Ahuja, R.; Xiong, Z.; Feng, Y.; Chen, P. Li⁺ Ion Conductivity and Diffusion Mechanism in α -Li₃N and β -Li₃N. *Energy Environ. Sci.* **2010**, *3*, 1524–1530.
- (65) Murugan, R.; Thangadurai, V.; Weppner, W. Fast Lithium Ion Conduction in Garnet-Type Li₇La₃Zr₂O₁₂. *Angew. Chem., Int. Ed.* **2007**, *46*, 7778–7781.